

Simulation of condensation flow in a rectangular microchannel



Si-han Chen^a, Zhen Yang^{a,*}, Yuanyuan Duan^{a,**}, Ying Chen^b, Di Wu^c

^a Key Laboratory for Thermal Science and Power Engineering of MOE, Beijing Key Laboratory for CO₂ Utilization and Reduction Technology, Tsinghua University, Beijing 100084, China

^b Faculty of Materials and Energy, Guangdong University of Technology, Guangzhou 510006, China

^c Ningbo Nuoke Electronic Technology Development Co., Ltd., Department of Oilfield Engineering, Bu Zheng Street, Zhejiang 315010, China

ARTICLE INFO

Article history:

Received 26 September 2012

Received in revised form 3 December 2013

Accepted 4 December 2013

Available online 15 December 2013

Keywords:

Simulation

VOF model

Two-phase flow

Condensation

Microchannel

Heat transfer

ABSTRACT

The condensation flow of the refrigerant FC-72 in a rectangular microchannel with a 1-mm hydraulic diameter is numerically studied using the volume of fluid (VOF) model. The heat transfer related to the condensation is taken into account by a thermal equilibrium model assuming the interface temperature is at saturation. The numerical method is validated against experiments from the literature and well predicts the flow patterns along the microchannel. The vapor phase in the microchannel forms a continuous column with a decreasing diameter from upstream to downstream. Slugs are periodically generated at the head of the column. Decreasing the wall cooling heat flux or increasing the flow mass flux increases the vapor column length. Waves along the interface cause necks in the column and locally increase the vapor velocity and decrease the pressure, facilitating breakage of the vapor column into slugs. The liquid temperature is close to saturation near the interface and lower downstream and in the thin liquid layer close to the cooling surface. The initial bubble size increases with increasing flow mass flux or decreasing cooling heat flux.

© 2013 Elsevier B.V. All rights reserved.

1. Introduction

Rapid developments in many cutting-edge technologies require efficient heat removal from areas subject to increasingly high heat fluxes. Examples include advanced electronics in computers, automobiles and aircraft. For heat fluxes exceeding 10,000 W m⁻², natural and forced convection with air and liquids are incapable of efficiently dissipating the heat; and device temperatures may rise above safe operating levels, resulting in devastating failures. Two-phase boiling flow in microchannels is a prominent candidate for heat transfer at extremely high heat fluxes above 10,000 W m⁻². With recent progress in manufacturing, microchannels can be fabricated in small regions exposed to high heat fluxes. Current fabrication methods include wire-sawing and chemical etching.

When heat is removed from the target device *via* microchannel boiling with two-phase flow in a cooling loop (called a primary loop here), the heat then needs to be efficiently rejected to a secondary loop and finally to the surroundings. Compact condensers, sometimes called micro-condensers, have microchannels arranged to

thermally connect the two loops to transfers heat from the primary loop to the secondary loop. Compact condensers are much smaller and less expensive than commercial macrochannel counterparts [1]. Compact condensers, for example with channel hydraulic diameters of 1.11 and 0.80 mm [2], have been successfully used in automobile air conditioners for decades [3]. The compact condenser is also used as one of the key components in micro-refrigeration systems [4–6].

On the primary loop side of a compact condenser, the refrigerant vapor from the hot target devices, is condensed into liquid in the microchannels with release of the latent heat in the refrigerant to the secondary loop side. Thus, condensation flow and heat transfer in the microchannels are central to the thermal performance of the compact condenser so they have attracted extensive academic and industrial interest. Yang and Web investigated R12 condensation flow in four parallel mini-channels with plain and micro-fin extruded tubes [7]. Yan and Lin [8], Wang et al. [9], and Koyama et al. [2] studied condensation heat transfer in parallel microchannels with hydraulic diameters of 0.81–2.0 mm. The flow patterns which determine the condensation heat transfer rate differ in microchannels from that in conventional macrochannels. Garimella et al. [10] developed a flow pattern map for condensation flow in circular microchannels with special interest on the intermittent flow regime. Hu and Cheng [11] reported on vapor injection flow and related condensation instabilities in microchannels. Hu and Chao [12] found that slug-bubbly flow was the dominant flow

* Corresponding author. Tel.: +86 10 6278 9751.

** Corresponding author. Tel.: +86 10 6279 6318.

E-mail addresses: zhenyang@tsinghua.edu.cn (Z. Yang), yyduan@tsinghua.edu.cn (Y. Duan).

Nomenclature

C_v	constant volume specific heat, $\text{J kg}^{-1} \text{K}^{-1}$
\bar{F}	momentum source term, $\text{N m}^{-3} \text{s}^{-1}$
g	acceleration due to gravity, m s^{-2}
h_{lv}	specific latent heat for liquid–vapor phase change, J kg^{-1}
\hat{i}	unit vector in the x direction, –
\hat{j}	unit vector in the y direction, –
\hat{k}	unit vector in the z direction, –
k	thermal conductivity, $\text{W m}^{-1} \text{K}^{-1}$
p	pressure, Pa
S_E	energy source term, $\text{J m}^{-3} \text{s}^{-1}$
S_l	mass source term for the liquid phase, $\text{kg m}^{-3} \text{s}^{-1}$
S_v	mass source term for the vapor phase, $\text{kg m}^{-3} \text{s}^{-1}$
T	temperature, K
t	time, s
\vec{v}	velocity vector, m s^{-1}

Greeks

α	volume fraction, –
μ	viscosity, $\text{kg m}^{-1} \text{s}^{-1}$
θ	contact angle, rad
ρ	density, kg m^{-3}
σ	surface tension, N m^{-1}

Subscripts

l	liquid phase
v	vapor phase
s	saturation

pattern and measured the heat transfer and pressure drop for water vapor condensation in a micro-condenser.

While the flow pattern and the associated heat transfer for microchannel condensation flows have been extensively explored using experimental observation and measurements, the details of the flow field, local temperature distribution and interface motion remain to be better understood. This constitutes the primary motivation for the present study. Numerical simulations supplementing experiment studies give additional details on the flow and heat transfer. The volume of fluid (VOF) model proposed by Hirt and Nichols [13] has been extensively used for two-phase flow simulations to track the liquid–vapor interface motion which strongly affects the two-phase flow and heat transfer in microchannels. Tomiyama et al. [14], Gopala and Wachem [15] and Jeon et al. [16] employed the VOF model to study a single rising bubble and found good agreement with experimental observations. The VOF model was also successfully used to study the velocity and local wall shear stress distributions around bubble slugs [17], coalescence of two bubbles [18] and the lift force on a bubble [19].

To take into account the heat and mass transfer at a liquid–vapor interface during phase change, mass and energy sources terms need to be defined in the continuum and energy equations of the VOF model. Yang et al. [20] used the VOF model with self-defined source terms to simulate the boiling flow of R141b in a serpentine tube, with the flow patterns found to agree well with their experiment observations. Huang et al. [21] studied bubble growth in R141b boiling flows in the coiled part of a serpentine tube using the VOF model with the simulations revealing the unusual contraction of bubbles due to the flow re-distribution induced by centrifugal forces in the bends, as was observed in their experiments. Da Riva and Del Col [22] used the VOF model to simulate R134a film condensation in a horizontal circular minichannel and found that the film thickness remained almost constant in the upper half of the

channel while the film in the bottom half became thicker due to gravity.

Although a number of studies have investigated condensation flows in microchannels, few have presented detailed flow and heat transfer results. The present study uses a VOF model with phase change to study condensation flow in microchannels. The model is first validated against existing experimental flow patterns from the open literature and then used to study FC-72 condensation flow for different mass fluxes and cooling heat fluxes. Detailed flow and temperature profiles are presented to give for a good understanding of the heat transfer mechanisms.

2. Mathematical modeling

2.1. VOF model

Even though the liquid–vapor interface changes its location and shape with time, the VOF model employs a fixed grid to model two-phase flows. The volume fraction of phase i in each cell is represented by α_i , with the sum of the volume fractions for all phases adding up to 1, i.e.:

$$\sum_i \alpha_i = 1 \quad (1)$$

In a liquid–vapor two-phase flow, when a cell is filled with liquid, the liquid volume fraction, α_l , is 1 and the corresponding vapor volume fraction, α_v , is 0. α_l is 0 and α_v is 1 when a cell is filled with vapor. If the cell is partially filled with liquid and the rest with vapor α_l and α_v are between 0 and 1, indicating that the interface passes through the cell.

The governing equations are as follows.

1. Continuity equation

$$\frac{\partial \alpha_i}{\partial t} + \vec{v} \nabla \alpha_i = \frac{S_i}{\rho_i} \quad (2)$$

where subscript i can either be l or v representing the liquid or vapor phase. S_i is the mass source term of phase i due to the phase change. ∇ is the gradient defined as $\nabla = \hat{i} \partial / \partial x + \hat{j} \partial / \partial y + \hat{k} \partial / \partial z$, where \hat{i} , \hat{j} and \hat{k} are the unit vectors in the x , y and z directions in the Cartesian coordinate system.

2. Momentum equation

$$\frac{\partial}{\partial t}(\rho \vec{v}) + \nabla \cdot (\rho \vec{v} \vec{v}) = -\nabla p + \nabla \cdot [\mu(\nabla \vec{v} + \nabla \vec{v}^T)] + \rho \vec{g} + \vec{F} \quad (3)$$

where ρ and μ are the mixture density and viscosity defined as:

$$\rho = \alpha_l \rho_l + \alpha_v \rho_v$$

and

$$\mu = \alpha_l \mu_l + \alpha_v \mu_v$$

Energy equation

$$\frac{\partial}{\partial t}(\rho E) + \nabla \cdot [\vec{v}(\rho E + p)] = \nabla \cdot [k_e \nabla T] + S_E \quad (4)$$

where S_E is the energy source term associated with the liquid–vapor phase change determined as:

$$S_E = h_{lv} S_l \quad (5)$$

E (J/kg) is the specific internal energy defined as:

$$E = \frac{\alpha_l \rho_l E_l + \alpha_v \rho_v E_v}{\alpha_l \rho_l + \alpha_v \rho_v}$$

where E_l and E_v are the specific internal energies of the liquid and vapor phases defined as:

$$E_i = C_{v,i}(T - T_s), \quad i = l \text{ or } v$$

where T_s is the saturation temperature at which the phase change occurs.

Parameter k_e in Eq. (4) is the effective thermal conductivity of the mixture defined as:

$$k_e = \alpha_l k_l + \alpha_v k_v$$

In the VOF model, the liquid and vapor velocities in Eqs. (3) and (4) are calculated using a single Eq. (3) as are the temperatures (Eq. (4)). This partly explains why the VOF model is a computationally efficient way to solve the momentum and energy equations.

2.2. Surface tension and contact angle

Surface tension arises from the difference in the molecular attractions between the two contacting phases which imposes a pressure jump across the interface when the interface is curved. The pressure jump across the interface can be converted to a volumetric force using the divergence theorem. This volumetric force is then applied to the interfacial cells ($0 < \alpha_i < 1$) by defining the source vector \vec{F} in Eq. (3) as [23]:

$$\vec{F} = \sigma \frac{2\rho(\nabla \cdot \hat{n})\nabla\alpha_i}{\rho_l + \rho_v}$$

where \hat{n} is the interface normal defined by $\hat{n} = \nabla\alpha_i / |\nabla\alpha_i|$.

The movement of the phase interface in the microchannels is largely affected by the contact angle at the channel wall. To model this effect, the interface normal \hat{n} in the cells adjacent to the wall is modified to:

$$\hat{n} = \hat{n}_w \cos \theta + \sqrt{1 - \hat{n}_w^2} \sin \theta$$

where \hat{n}_w is the unit vector normal to the wall and θ is the contact angle.

2.3. Phase change at the interface

The liquid–vapor phase change occurring at the interface is accompanied by mass transport between the two phases and the release (in condensation) or absorption (in evaporation) of latent heat. To account for the mass and heat transfer related to the phase change, the mass and heat sources in the governing equations are defined as [20]:

$$\begin{aligned} \text{Liquid mass source : } S_l &= \begin{cases} f_0 \rho_v \alpha_v (T_s - T), & \text{if } T < T_s \\ f_0 \rho_l \alpha_l (T_s - T), & \text{if } T > T_s \end{cases} \\ \text{Vapor mass source : } S_v &= \begin{cases} -f_0 \rho_v \alpha_v (T_s - T), & \text{if } T < T_s \\ -f_0 \rho_l \alpha_l (T_s - T), & \text{if } T > T_s \end{cases} \end{aligned} \quad (6)$$

where f_0 is an adjustable parameter which will be discussed in a later section. It is noted that S_l and S_v must sum to zero for mass conservation, indicating the mass gained/lost by one phase should equal that lost/gained by the other phase. Then, the associated heat source is readily obtained via Eq. (5). Note that the source terms defined in Eq. (6) are zero for a subcooled liquid ($\alpha_l = 1$, $\alpha_v = 0$, $T < T_s$) and a superheated vapor ($\alpha_l = 0$, $\alpha_v = 1$, $T > T_s$), indicating that no phase change occurs in these two cases. These terms are nonzero at an interface in a thermal non-equilibrium region ($0 < \alpha_l, \alpha_v < 1$, $T \neq T_s$), in a subcooled vapor ($\alpha_l = 0$, $\alpha_v = 1$, $T < T_s$) and in a superheated liquid ($\alpha_l = 1$, $\alpha_v = 0$, $T > T_s$), indicating that phase change can occur in these conditions.

The physical significance of Eq. (6) is that the temperature difference relative to the saturation temperature is the driving force for phase change at the interface, and near saturation the phase change rate is approximately linearly related to the temperature difference. For normal conditions, the thermal resistance due to the

phase change is extremely small compared to those due to conduction and convection so the temperature difference at the interface, i.e., $T_s - T$, can be safely neglected and $T \approx T_s$. To satisfy $T \approx T_s$ the coefficient f_0 in Eq. (6) was tuned to narrow the temperature difference between T and T_s to negligibly small values. Initial calculations showed that increasing f_0 effectively reduced the temperature difference but resulted in instabilities in the calculation. After many tries, f_0 is finally set to $100 \text{ (s}^{-1} \text{ K}^{-1})$ for the given mesh and time step with the temperature difference well controlled to within 0.1 K and the calculation remaining stable.

2.4. Grid and boundary conditions

The microchannel of interest had a rectangular cross-section of $1 \text{ mm} \times 1 \text{ mm}$ and a length of 300 mm. This particular geometry was chosen because rectangular channels with hydraulic diameters around 1 mm can be economically fabricated using wire-sawing, they are extensively used in heat sinks for chip cooling, and sufficient experimental data are available for model validation [1]. Fig. 1 shows the microchannel geometry and grid used for the simulations. The grid independence of the calculations was first checked before carrying out extensive case studies by doubling the number of elements and halving the time step with changes of less than 0.5% in the mean bottom wall temperature and less than 1% in the maximum local wall temperature in the fully developed flow stage. Thus, the mesh and time step were deemed to be sufficiently accurate and suitable for further simulations. The adopted grid had around 200,000 cells and the time step was $1 \times 10^{-6} \text{ s}$. The boundary conditions corresponding to the experimental conditions [1] are set as follows.

At the inlet, saturated vapor enters the channel at a fixed mass flowrate; therefore, the boundary conditions are:

$$\vec{v} = v\vec{k}, \quad T = T_s, \quad \alpha_v = 1, \quad \alpha_l = 0, \quad Q_m = \int_{A_{in}} \rho_v v dA \quad (7)$$

where Q_m is the mass flowrate, A_{in} is the inlet area and \vec{k} is the unit vector in the z direction (flow direction).

At the outlet, the flow and heat transfer are assumed to be fully developed so the derivatives of all the scalars along the flow direction are set to zero: (8) $\frac{\partial \vec{v}}{\partial z} = 0$, $\frac{\partial T}{\partial z} = 0$, $\frac{\partial \alpha_v}{\partial z} = 0$, $\frac{\partial \alpha_l}{\partial z} = 0$

At the bottom and side walls, heat is removed. In most of the experiments, the side walls acted as fins so the cooling heat flux was not the same as on the bottom wall. However, to simplify the calculations a uniform heat flux is assumed at the bottom and side walls. The boundary conditions are then:

$$\vec{v} = 0 \quad \frac{\partial \alpha_v}{\partial n} = 0 \quad \frac{\partial \alpha_l}{\partial n} = 0 \quad \frac{\partial T}{\partial n} = \frac{q}{k_e} \quad (9)$$

where q is the wall cooling heat flux.

In most of the experiments, the top wall was a glass cover exposed to air for flow observations [1,11]. Since the heat loss induced by natural convection is much less than the heat dissipated by cooling on the bottom and side walls, the top wall is treated as an adiabatic boundary, thus:

$$\vec{v} = 0 \quad \frac{\partial \alpha_v}{\partial n} = 0 \quad \frac{\partial \alpha_l}{\partial n} = 0 \quad \frac{\partial T}{\partial n} = 0 \quad (10)$$

2.5. Solution

The computational domain was discretized into hexahedral cells. The second-order upwind scheme was used for the convective fluxes, with central-differencing used to discretize the diffusion fluxes. A second-order implicit scheme was used for the time discretization. The PISO algorithm was used for the pressure–velocity coupling [24]. The iterations at each time step were terminated

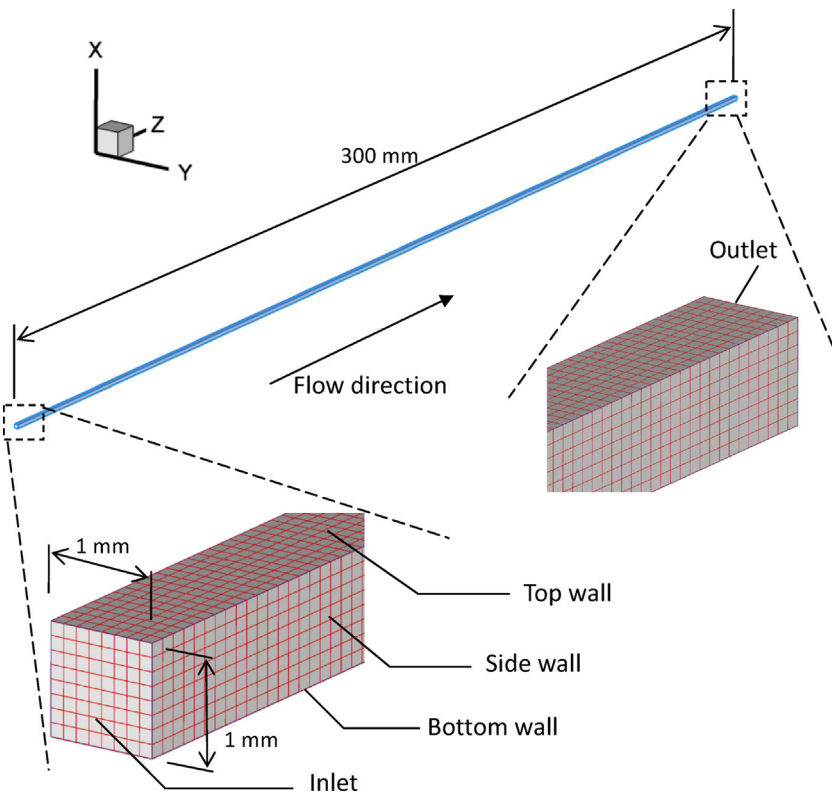


Fig. 1. Microchannel structure and computational grid.

when the dimensionless residuals for all the equations dropped below 10^{-3} . The computations were performed using the commercial software package, FLUENT 6.1 [25]. User-defined functions (UDFs) were developed for the source terms in Eqs. (2) and (4). The flow turbulence was modeled using the realizable $k-\varepsilon$ model [26] since this model is believed to provide superior performance for complex flows [25] and has been used and validated in previous studies [20,21].

3. Model validation

Before the extensive case studies, the model was first validated against available experimental data. This was done by examining the flow patterns for different regimes of microchannel condensation flow. Kim et al. [1] experimentally studied the condensation flow of FC-72 in parallel, square microchannels with a hydraulic diameter of 1 mm and a length of 29.9 cm with sufficient details on flow patterns for specific flow and thermal conditions. Since the channel structure is exactly the same as in the current study, their experimental results can be used to validate the present model.

Fig. 2 compares the experimental and simulated condensation flow patterns at $G=68 \text{ kg m}^{-2} \text{ s}^{-1}$ and $q=8500 \text{ W m}^{-2}$. The flow direction is from left to right. The flow patterns are shown for five different distances from the inlet along the channel from the top to the bottom in Fig. 2. The simulated flow patterns agree reasonably well with the experimental observations in each flow regime. In particular, the generation of the vapor slug (at $z=9.4 \text{ cm}$ in the simulation in Fig. 2), which is important in microchannel two-phase flows, is well predicted by the simulation. This provides good confidence in further studies using the present model.

A more comprehensive comparison of the flow regimes is shown in Fig. 3. As seen, the simulation results for the regime transitions are close to the regime borders (the regime transition lines) defined by Kim et al. [1], as well as their experimental data, showing that

predictions are reasonably good. The results differ from the regime borders defined by Wang et al. [9] probably because that the current channel geometry (hydraulic diameter 1 mm) and refrigerant (FC-72), which are the same as in the experiments of Kim et al., differ from those used by Wang et al. (hydraulic diameter 1.46 mm and R134a).

4. Results and discussion

The validated model was then used to study the flow and heat transfer details for the FC-72 condensation two-phase flow in the microchannel, including the flow patterns, velocity and temperature profiles and the slug flow. FC-72 is a dielectric fluid which can be safely used for heat transfer in electronic devices without the risk of electrical short-circuits. FC-72 has a saturation temperature of 56°C at atmospheric pressure which is $10\text{--}20^\circ\text{C}$ above common environmental temperatures so it is suitable for heat dissipation.

Typical thermophysical properties of FC-72 at $T_s=60^\circ\text{C}$ are listed in Table 1 [1]. The heat fluxes ranged from $10,000$ to $30,000 \text{ W m}^{-2}$ as in previous studies [1,9]; and the mass fluxes of interest were $100\text{--}150 \text{ kg m}^{-2} \text{ s}^{-1}$ which is in the ranges used in Kim et al. [1].

4.1. Flow patterns

The microchannel condensation two-flow patterns have been a major interest in many studies [11,12,27–29]; however, our understanding of the underlying mechanisms is still very limited relative to that in macro-channels [30,31]. As the channel size decreases, the impact of interface surface tension force on the condensation flow pattern becomes increasingly important. Fig. 4 shows the flow patterns of the FC-72 condensation flows at a mass flux of $G=100 \text{ kg m}^{-2} \text{ s}^{-1}$. These flow patterns are for relatively low vapor qualities ($x<0.5$), including the transition from two-phase flow to

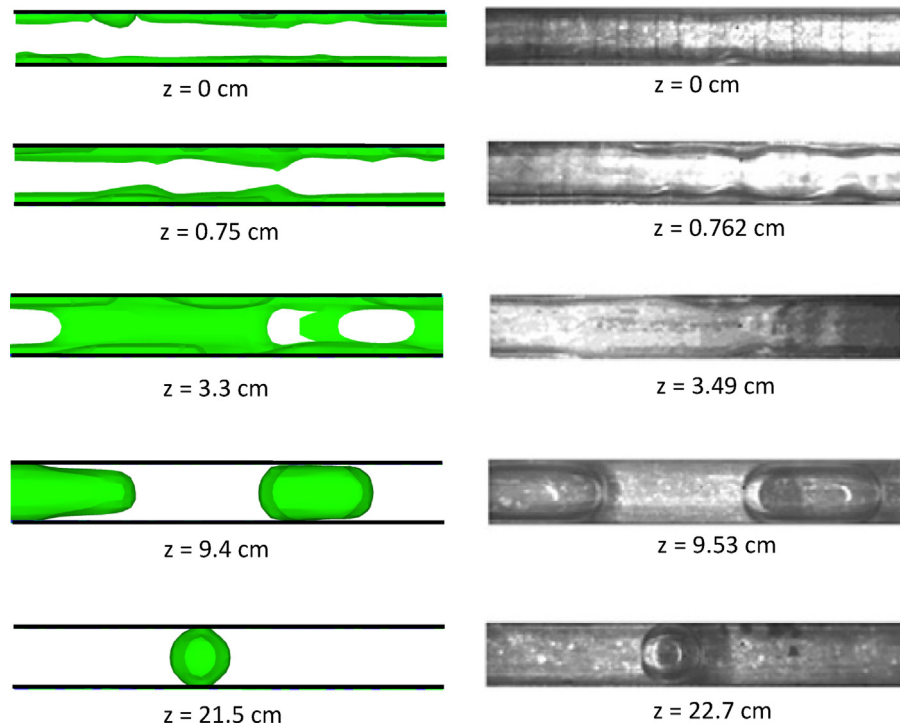


Fig. 2. Flow patterns predicted by the present model (left) and seen experimentally (right) [1] at five different flow distances for $G = 68 \text{ kg m}^{-2} \text{ s}^{-1}$ and $q = 8500 \text{ W m}^{-2}$. The flow direction is from left to right. From the top to the bottom, the figures show smooth annular flow, wavy annular flow, transition flow, slug flow and bubbly flow.

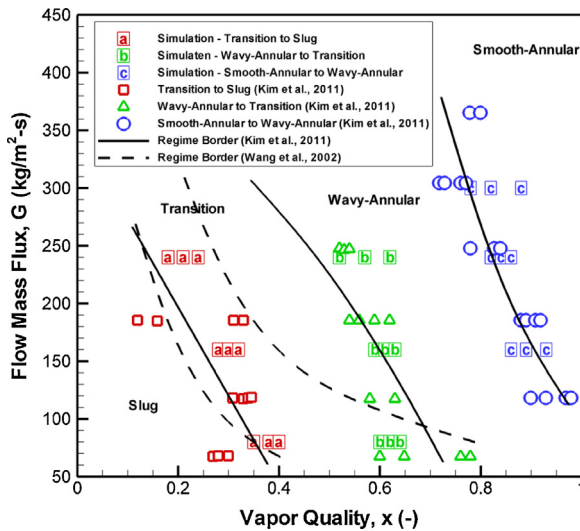


Fig. 3. Comparison of present simulation flow regime data with those of Kim et al. [1] and Wang et al. [9]. The data of Kim et al. is for FC-72 condensation flows in a rectangular channel of hydraulic diameter 1 mm with the data of Wang et al. is for R134a condensation flows in a rectangular channel of hydraulic diameter 1.46 mm.

single-phase liquid flow. A continuous vapor column is formed by the condensation with its diameter decreasing from upstream to downstream as the vapor continuously condenses into liquid. Bubbles are periodically generated at the head of the column, as shown in Figs. 4(a), 5(b) and (c). Bubbles are not seen in Fig. 4(b) and (c)

because they disappeared right at this moment before new ones were generated. Fig. 5(a) has no bubbles but liquid films and patches formed on the microchannel walls. In this case, the vapor is not sufficiently condensed into liquid before it exits the channel due to the low cooling rate ($q = 10,000 \text{ W m}^{-2}$) and the large vapor flow velocity ($G = 150 \text{ kg m}^{-2} \text{ s}^{-1}$).

Increasing the cooling heat flux to $30,000 \text{ W m}^{-2}$ shortens the vapor column length, as noted from the different flow distances (the values of z) in Figs. 4 and 5. For instance, since the cooling heat flux is smallest in Fig. 4(a), the vapor column head is furthest downstream at $z = 240 \text{ mm}$, quite close to the exit ($z = 300 \text{ mm}$). On the contrary, the head is furthest upstream at $z = 70 \text{ mm}$ with the largest heat flux in Fig. 4(c). Gravity causes the vapor to tend to float up and attach to the top wall, as seen from the bubble slug in front of the vapor column in Fig. 4(a).

The flow pattern also changes as the flow mass flux increases. Fig. 5 shows flow patterns at $G = 150 \text{ kg m}^{-2} \text{ s}^{-1}$ for different cooling heat fluxes. The increase in the flow mass flux enhances the friction at the interface between the vapor and liquid which causes more violent waves along the interface, as shown by comparing Figs. 4 and 5 where the interfaces in Fig. 4 are smoother than those in Fig. 5. The waves could lead to break-up of the vapor column and cause the flow regime to change from transition flow to slug flow, which will be further discussed in later sections.

Another direct result of increasing the flow mass flux is that the vapor column head extends further downstream. For example, at a fixed cooling heat flux of $20,000 \text{ W m}^{-2}$ the column head is at $z = 110 \text{ mm}$ with a flow mass flux of $G = 100 \text{ kg m}^{-2} \text{ s}^{-1}$ while it extends to $z = 180 \text{ mm}$ with a increased flow mass flux of

Table 1
Thermophysical properties of FC-72 at $T_s = 60^\circ \text{C}$ [1].

$h_{lv} \text{ (kJ kg}^{-1}\text{)}$	$\rho_l \text{ (kg m}^{-3}\text{)}$	$\rho_v \text{ (kg m}^{-3}\text{)}$	$\mu_l \text{ (kg m}^{-1} \text{ s}^{-1}\text{)}$	$k_l \text{ (W m}^{-1} \text{ K}^{-1}\text{)}$	$C_{p,l} \text{ (kJ kg}^{-1} \text{ K}^{-1}\text{)}$	$\sigma \text{ (mN m}^{-1}\text{)}$
93.7	1583.4	14.90	4.18×10^{-4}	0.0534	1.1072	8.0

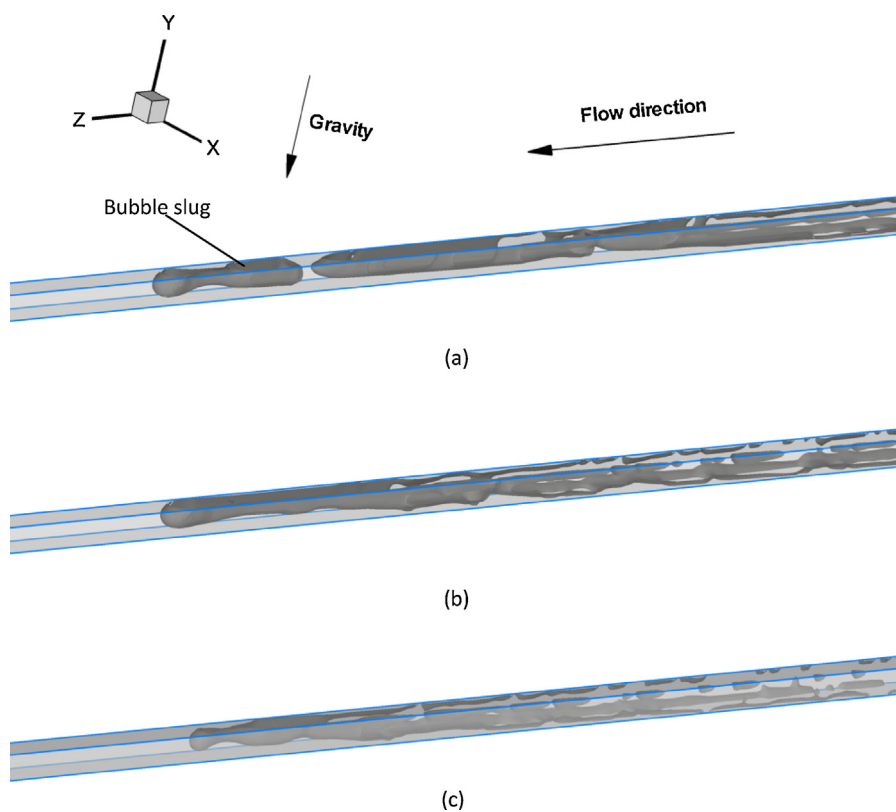


Fig. 4. Flow patterns for $G = 100 \text{ kg m}^{-2} \text{ s}^{-1}$: (a) $q = 10,000 \text{ W m}^{-2}$, $z = 240 \text{ mm}$; (b) $q = 20,000 \text{ W m}^{-2}$, $z = 110 \text{ mm}$; (c) $q = 30,000 \text{ W m}^{-2}$, $z = 70 \text{ mm}$.

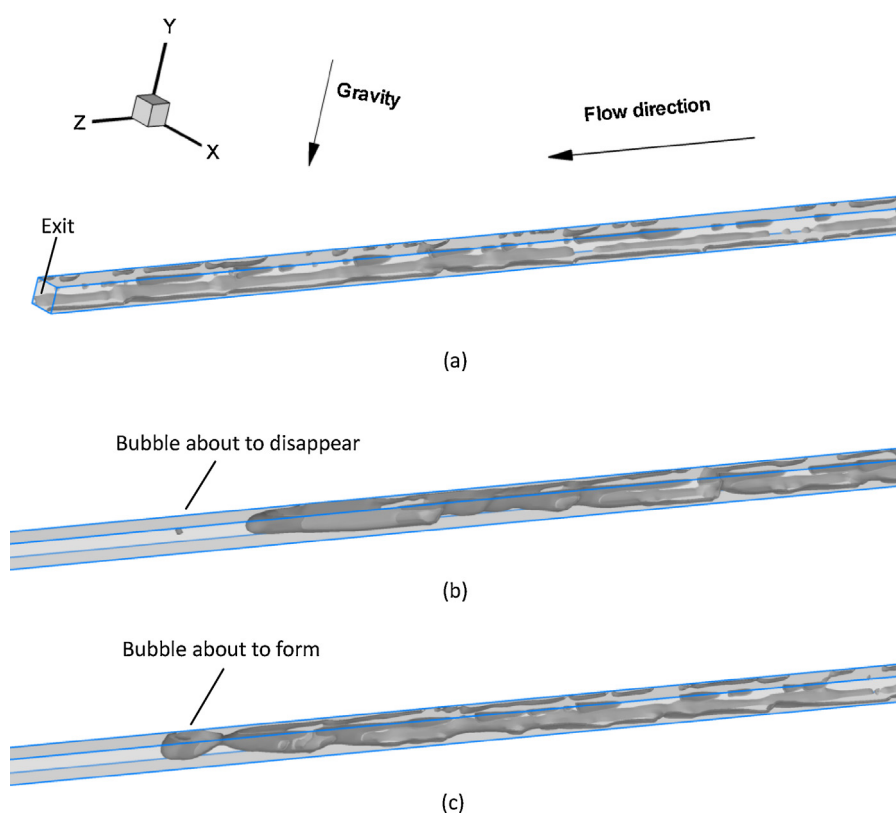


Fig. 5. Flow patterns for $G = 150 \text{ kg m}^{-2} \text{ s}^{-1}$: (a) $q = 10,000 \text{ W m}^{-2}$, $z = 280 \text{ mm}$; (b) $q = 20,000 \text{ W m}^{-2}$, $z = 180 \text{ mm}$; (c) $q = 30,000 \text{ W m}^{-2}$, $z = 110 \text{ mm}$.

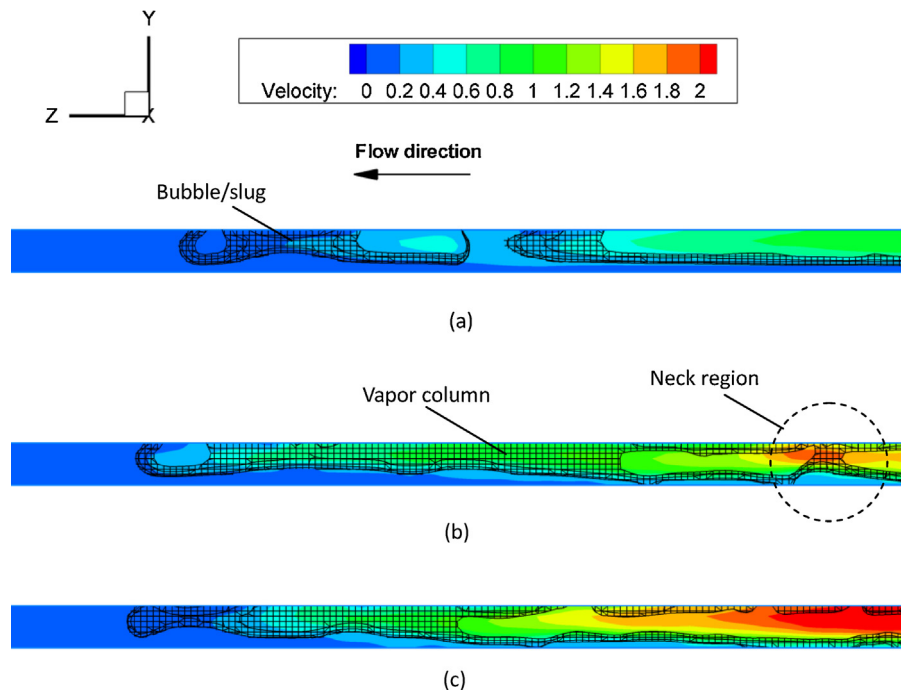


Fig. 6. Velocities (m s^{-1}) for $G = 100 \text{ kg m}^{-2} \text{ s}^{-1}$ (interfaces are shown by the grid lines): (a) $q = 10,000 \text{ W m}^{-2}$, $z = 240 \text{ mm}$; (b) $q = 20,000 \text{ W m}^{-2}$, $z = 110 \text{ mm}$; (c) $q = 30,000 \text{ W m}^{-2}$, $z = 70 \text{ mm}$.

$G = 150 \text{ kg m}^{-2} \text{ s}^{-1}$, as shown in Figs. 4(b) and 5(b). The column head even extends out of the channel when the heat flux is sufficiently low, e.g., at $10,000 \text{ W m}^{-2}$, as seen in Fig. 5(a).

4.2. Flow and temperature fields

Condensation of vapor to liquid reduces the volume and releases latent heat, which significantly impacts the flow and temperature fields. Fig. 6 shows the flow velocity profiles on the vertical middle plane of the microchannel. The velocity decreases from upstream to downstream as the vapor condenses. Also, the flow velocities are much larger in the vapor column than in the adjacent liquid region; thus, a large sliding velocity exists between the two phases. In the slugs, the vapor velocities are significantly lower than in the vapor column, as shown by comparing the velocity magnitudes in the slug with those in the rear vapor column in Fig. 5(a).

The waves along the interface have an important impact on the local vapor velocity. The wavy interface causes necks to form in the vapor column, resulting in acceleration of the local vapor flow, as shown by the neck region in Fig. 6(b). This acceleration causes a drop in the local pressure according to Bernoulli's Law, which helps further narrow the neck and leads to breakage of the vapor column into slugs when the neck is sufficiently thin.

Fig. 7 shows the temperature profiles on the vertical middle plane of the microchannel for flows at $G = 100 \text{ kg m}^{-2} \text{ s}^{-1}$. During condensation, the latent heat is continuously released, which prevents the temperature from dropping at the interface and keeps the adjacent fluid temperatures close to saturation, as evident by the uniform, high-temperature zones in the vapor column and in the nearby liquid regions in Fig. 7. Significant temperature gradients are only found in the liquid region downstream of the vapor column and in the thin liquid layer close to the cooling surfaces (the bottom and side walls), as seen in Fig. 7. Increasing the cooling heat flux shrinks the high-temperature area downstream of the vapor column due to increased heat dissipation by the cooling walls, as shown by comparison of the flows at different heat fluxes in Fig. 7.

Fig. 8 shows the temperature profiles on the vertical middle plane of the microchannel for flows at a larger flow mass flux of $G = 150 \text{ kg m}^{-2} \text{ s}^{-1}$. Comparing Fig. 8 to Fig. 7 shows that increasing the flow mass flux and, thus, the flow velocity greatly expands the high-temperature area downstream of the vapor column, as shown in Figs. 7(b), 8(b) and 7(c), 8(c). At a larger flow mass flux, convection becomes more important and drives the high-temperature liquid further downstream. This leads to expansion of the high-temperature area in front of the vapor column. Additionally, the bubbles that break away from the vapor column release their latent heat as they flow further downstream, which also helps to expand the high-temperature area in front of the vapor column, as seen in Fig. 8(b).

4.3. Slug flow

Slug flow is a prominent flow pattern in microchannel two-phase flows [11,12]. Slugs are separate from the vapor column via a process during which the vapor column locally contracts until break-up. Fig. 9 shows the formation of a slug in the microchannel. At $t = 0 \text{ ms}$, a vapor slug is about to separate from the vapor column with only a thin neck. As the neck breaks, a slug forms (Fig. 9b). Then, the slug flows downstream and releases its latent heat to the surrounding liquid so its volume decreases (Fig. 9c) as the inside vapor condenses into liquid.

Bubble volume histories were further analyzed for different conditions. Fig. 10 shows the changes in the bubble volume for 5 different cases. The bubble volumes were calculated after the flows were fully developed and bubbles were periodically generated. The case with $G = 150 \text{ kg m}^{-2} \text{ s}^{-1}$ and $q = 10,000 \text{ W m}^{-2}$ is not included because slugs did not form due to insufficient condensation at this relatively large flow velocity and relatively small heat flux. In each case, the bubble volume decreased with time with the rate of decrease slowing downstream. Immediately after separation, the bubble is relatively large with a large interfacial area for condensation. This results in a relatively higher rate of volume

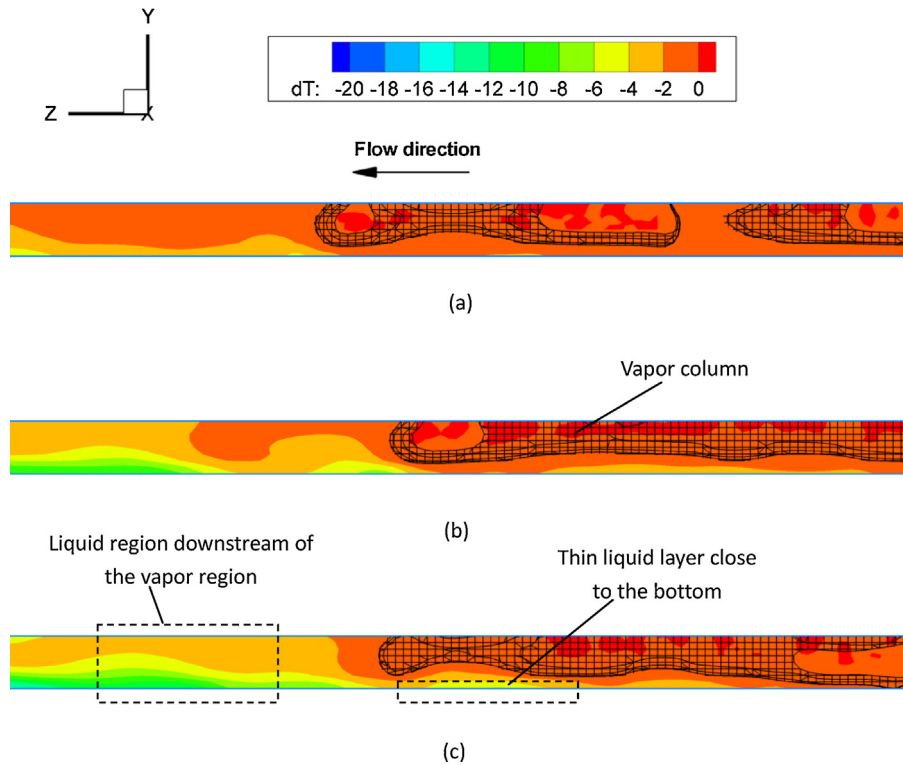


Fig. 7. Temperature ($dT = T - T_s$, K) distributions for $G = 100 \text{ kg m}^{-2} \text{ s}^{-1}$ (interfaces are shown by the grid lines): (a) $q = 10,000 \text{ W m}^{-2}$, $z = 240 \text{ mm}$; (b) $q = 20,000 \text{ W m}^{-2}$, $z = 110 \text{ mm}$; (c) $q = 30,000 \text{ W m}^{-2}$, $z = 70 \text{ mm}$.

decrease initially. As the bubble size decreases, the interfacial area also decreases as does the bubble volume decrease rate.

The initial bubble volume at $t = 0 \text{ ms}$ is dependent upon the heat and flow mass fluxes. At the flow mass flux of $100 \text{ kg m}^{-2} \text{ s}^{-1}$, the initial bubble size is largest (4.5 mm^3) with the smallest heat flux of 10 kW m^{-2} and smallest (0.6 mm^3) with the largest heat flux of 30 kW m^{-2} , as seen in Fig. 10. This indicates that larger slugs are

formed at smaller heat fluxes. This may be explained as follows. At a small heat flux, the vapor is condensed at a relatively low rate and the vapor column can stretch far along the microchannel. For instance, the vapor column spans from the inlet at $z = 0 \text{ mm}$ to $z = 240 \text{ mm}$ with the smallest heat flux of $q = 10 \text{ kW m}^{-2}$, while only extends to $z = 70 \text{ mm}$ with the largest heat flux of $q = 30 \text{ kW m}^{-2}$, as seen in Fig. 4. A long vapor column also results in a long, low-vapor

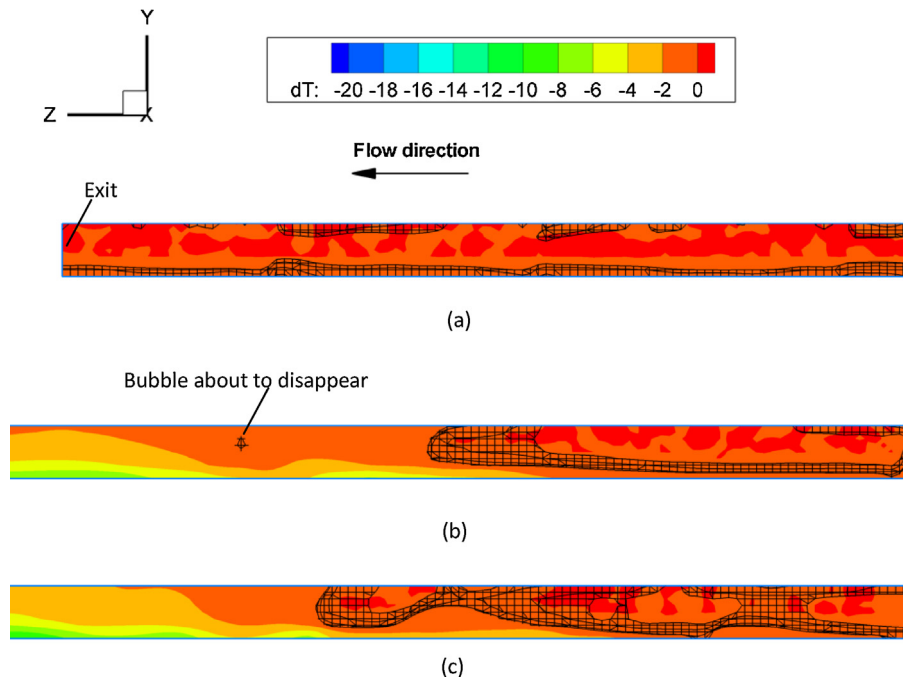


Fig. 8. Temperature ($dT = T - T_s$, K) distributions for $G = 150 \text{ kg m}^{-2} \text{ s}^{-1}$ (interfaces are shown by the grid lines): (a) $q = 10,000 \text{ W m}^{-2}$, $z = 280 \text{ mm}$; (b) $q = 20,000 \text{ W m}^{-2}$, $z = 180 \text{ mm}$; (c) $q = 30,000 \text{ W m}^{-2}$, $z = 110 \text{ mm}$.

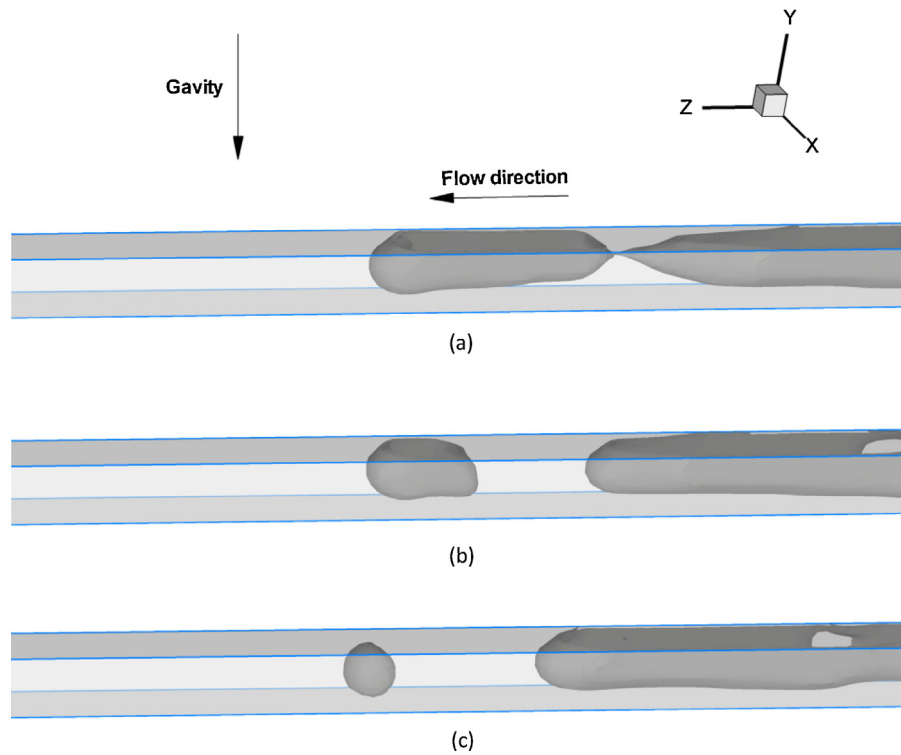


Fig. 9. Slug flow for $G = 100 \text{ kg m}^{-2} \text{ s}^{-1}$ and $q = 20,000 \text{ W m}^{-2}$: (a) $t = 0 \text{ ms}$; (b) $t = 8.2 \text{ ms}$ and (c) $t = 16.3 \text{ ms}$.

quality region, e.g., the region with $x < 0.1$. Since slugs are formed from breaks in the vapor column in the low-vapor quality region, a longer low quality region will increase the possibility of formation of large slugs. This leads to large slugs being formed in flows with small heat fluxes.

Similar to the effect of decreasing the heat flux, increasing the flow mass flux also results in expansion of the vapor column. For instance, the vapor column spans from $z = 0 \text{ mm}$ to $z = 180 \text{ mm}$ for $G = 150 \text{ kg m}^{-2} \text{ s}^{-1}$ in Fig. 5(b), but only extends to $z = 110 \text{ mm}$ for $G = 100 \text{ kg m}^{-2} \text{ s}^{-1}$ in Fig. 4(b). As stated, longer vapor columns produce larger slugs. Therefore, increasing the flow mass flux leads to an increase in the vapor column length and, thus, an increase in the initial bubble volume. For instance, at the same heat flux of 20 kW m^{-2} the initial bubble volume for $G = 100 \text{ kg m}^{-2} \text{ s}^{-1}$ is only

2.1 mm^3 , while it is increased to 4.7 mm^3 for $G = 150 \text{ kg m}^{-2} \text{ s}^{-1}$, as shown in Fig. 10.

Fig. 11 shows the bubble velocities after separation. These velocities were obtained by measuring the positions of the bubble geometric center at different times. At the separation point, the interface is distorted significantly at the neck, as shown in Fig. 9(a). After separation, the slug quickly recovers its round shape due to the influence of surface tension. The fast change in the slug shape results in flow disturbances in the adjacent liquid, causing oscillations in the bubble velocity as seen in Fig. 11.

Fig. 11 also shows that the velocities of the larger bubbles generally decrease with time. For instance, the velocity of the bubble (initial size 4.8 mm^3) in the flow for $G = 150 \text{ kg m}^{-2} \text{ s}^{-1}$ and $q = 20 \text{ kW m}^{-2}$ drops from 0.27 m s^{-1} to about 0.15 m s^{-1} . A similar

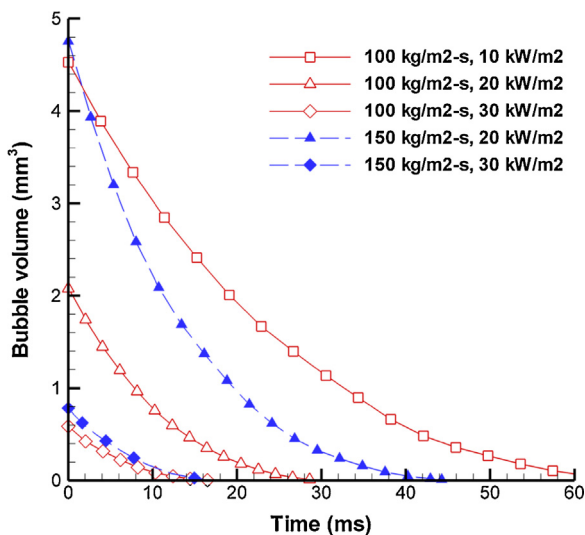


Fig. 10. Bubble volume shrinkage after separation from the vapor column.

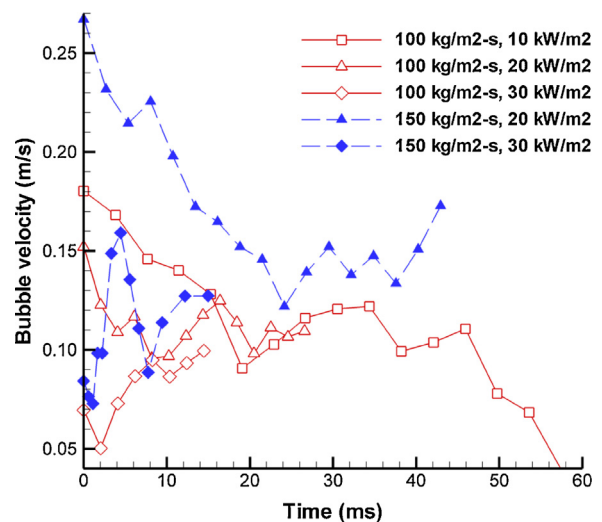


Fig. 11. Bubble velocities after separation from the vapor column.

trend is observed for the bubble (initial size 4.5 mm^3) in the flow for $G = 100 \text{ kg m}^{-2} \text{ s}^{-1}$ and $q = 10 \text{ kW m}^{-2}$. Large bubbles are longer with larger interfaces; therefore, the vapor condensation is relatively high as is the volume reduction due to the condensation. The drastic volume reduction enhances the internal vapor flow toward the bubble center which causes a relatively large velocity zone inside the bubble, as evident from the zone of relatively large velocities in the rear part of the slug in Fig. 6(a). As a result, the bubble velocity is initially large. As the slug size decreases during condensation, the interfacial area decreases with the volume contraction. This reduces the vapor velocities inside the bubble and then the slug velocity. For small bubbles, e.g., the bubble with an initial size of 0.6 mm^3 for $G = 100 \text{ kg m}^{-2} \text{ s}^{-1}$ and $q = 30 \text{ kW m}^{-2}$, the effect of the volume contraction is not evident so no reduction in the bubble velocity is found, as shown by the line for $G = 100 \text{ kg m}^{-2} \text{ s}^{-1}$ and $q = 30 \text{ kW m}^{-2}$ in Fig. 11.

5. Conclusions

A two-phase VOF model with phase change was used to study condensation flow of FC-72 in a rectangular microchannel with a hydraulic diameter of 1 mm. The simulated flow patterns, including bubbly flow, slug flow, transition flow, wavy annular flow and smooth annular flow regimes, agree well with experimental observations.

In the microchannel, the vapor phase forms a continuous column with a decreasing diameter downstream. Slugs are periodically generated at the head of the column. Decreasing the wall cooling heat flux and increasing the flow mass flux both increase the vapor column length.

During condensation, the vapor velocity decreases downstream but is significantly higher than the adjacent liquid velocity. The vapor velocity inside the bubbles is lower than in the upstream vapor column. Waves along the interface form necks that locally increase the vapor velocity and decrease the pressure. The liquid temperatures near the interface remain near saturation due to large release of latent heat with low temperatures in the liquid downstream of the vapor column and in the thin liquid layer close to the cooling walls.

The initial bubble size increases as the flow mass flux increases or the heat flux decreases. After separation, the larger bubbles tend to slow due to the decreased condensation rate resulting from a decrease in the interfacial area.

Use of this model to study the heat transfer coefficient on the cooling walls is still difficult due to the high computational costs imposed by the need for a fine grid in the thin liquid film. This problem may be solved by developing sub-models to bridge the heat transfer between the thin liquid layer and the mainstream vapor. This work will be conducted in future studies.

Acknowledgements

The authors acknowledge financial support from the National Natural Science Foundation of China (Nos. U0934006 and 51106083) and Science Fund for Creative Research Groups (No. 51321002).

References

- [1] S.M. Kim, J. Kim, I. Mudawar, Flow condensation in parallel micro-channels – Part 1: experimental results and assessment of pressure drop correlations, *Int. J. Heat Mass Transf.* 55 (2012) 971–983.
- [2] S. Koyama, K. Kuwahara, K. Nakashita, K. Yamamoto, An experimental study on condensation of refrigerant R134a in a multi-port extruded tube, *Int. J. Refrig.* 24 (2003) 425–432.
- [3] H.S. Wang, J.W. Rose, Theory of heat transfer during condensation in microchannels, *Int. J. Heat Mass Transf.* 54 (2011) 2525–2534.
- [4] T.A. Ameel, R.O. Warrington, R.S. Wegeng, M.K. Drost, Miniaturization technologies applied to energy systems, *J. Energy Convers. Manage.* 38 (1996) 969–982.
- [5] S.T. Munkejord, H.S. Mæhlum, G.R. Zakeri, P. Neksa, Micro technology in heat pumping systems, *Int. J. Refrig.* 25 (2002) 471–478.
- [6] S. Jeong, How difficult is it to make a micro refrigerator? *Int. J. Refrig.* 27 (2002) 309–313.
- [7] C.Y. Yang, R.L. Webb, Condensation of R-12 in small hydraulic diameter extruded aluminum tubes with and without micro-fins, *Int. J. Heat Mass Transf.* 39 (1996) 791–800.
- [8] Y.Y. Yan, T.F. Lin, Condensation heat transfer and pressure drop of refrigerant R-134a in a small pipe, *Int. J. Heat Mass Transf.* 42 (1999) 697–708.
- [9] W.W. Wang, T.D. Radcliff, R.N. Christensen, A condensation heat transfer correlation for millimeter-scale tubing with flow regime transition, *Exp. Therm. Fluid Sci.* 26 (2002) 473–485.
- [10] S. Garimella, J.D. Killian, J.W. Coleman, An experimentally validated model for two-phase pressure drop in the intermittent flow regime for circular microchannels, *J. Fluid Eng.-T. ASME* 125 (5) (2003) 887–894.
- [11] H.Y. Wu, P. Cheng, Condensation flow patterns in silicon microchannels, *Int. J. Heat Mass Transf.* 48 (2005) 2186–2197.
- [12] J.S. Hu, C.Y.H. Chao, An experimental study of the fluid flow and heat transfer characteristics in micro-condensers with slug-bubbly flow, *Int. J. Refrig.* 30 (2007) 1309e–1318e.
- [13] C.W. Hirt, B.D. Nichols, Volume of fluid (VOF) method for the dynamics of free boundaries, *J. Comput. Phys.* 39 (1981) 201–225.
- [14] A. Tomiyama, A. Sou, H. Minagawa, T. Sakaguchi, Numerical analyses of a single bubble by VOF method, *Jpn Soc. Mech. Eng.* 36 (1993) 51–56.
- [15] V.R. Gopala, B.G.M. Wachem, Volume of fluid methods for immiscible-fluid and free-surface flows, *Chem. Eng. J.* 141 (2008) 204–221.
- [16] S.S. Jeon, S.J. Kim, G.C. Park, Numerical study of condensing bubble in subcooled boiling flow using volume of fluid model, *Chem. Eng. Sci.* 66 (2011) 5899–5909.
- [17] T. Taha, Z.F. Cui, CFD modeling of slug flow in vertical tubes, *Chem. Eng. Sci.* 61 (2006) 676–687.
- [18] M.S. Annaland, N.G. Deen, J.A.M. Kuipers, Numerical simulation of gas bubbles behavior using a three-dimensional volume of fluid method, *Chem. Eng. Sci.* 60 (2005) 2999–3011.
- [19] S.S. Rabha, V.V. Buwa, Volume-of-fluid (VOF) simulations of rise of single/multiple bubbles in sheared liquids, *Chem. Eng. Sci.* 65 (2009) 527–537.
- [20] Z. Yang, X.F. Peng, P. Ye, Numerical and experimental investigation of two phase flow during boiling in a coiled tube, *Int. J. Heat Mass Transf.* 51 (2008) 1003–1016.
- [21] M. Huang, Z. Yang, Y.Y. Duan, D.J. Lee, Bubble growth for boiling bubbly flow for R141b in a serpentine tube, *J. Taiwan Inst. Chem. Eng.* 42 (2011) 727–734.
- [22] E. Da Riva, D. Del Col, Numerical simulation of laminar liquid film condensation in a horizontal circular minichannel, *J. Heat Trans. T-ASME* 134 (2012) 051019.
- [23] J.U. Brackbill, D.B. Kothe, C. Zemach, A continuum method for modeling surface tension, *J. Comput. Phys.* 100 (1992) 335–354.
- [24] R.I. Issa, Solution of implicitly discretized fluid flow equations by operator splitting, *J. Comput. Phys.* 62 (1986) 40–65.
- [25] ANSYS Inc., Fluent 6.3 User's Guide, ANSYS Inc., Lebanon, NH, 2006 <http://www.ansys.com/>
- [26] T.H. Shih, W.W. Liou, A. Shabbir, Z. Yang, J. Zhu, A new $k-\epsilon$ eddy-viscosity model for high Reynolds number turbulent flows: model development and validation, *Comput. Fluids* 24 (1995) 227–238.
- [27] H. Wang, J.W. Rose, Film condensation in horizontal microchannels: effect of channel shape, *Int. J. Therm. Sci.* 45 (2006) 1205–1212.
- [28] T.S. Zhao, Q. Liao, Theoretical analysis of film condensation heat transfer inside vertical mini triangular channels, *Int. J. Heat Mass Transf.* 45 (13) (2002) 2829–2842.
- [29] Y. Chen, P. Cheng, Condensation of steam in silicon microchannels, *Int. Commun. Heat Mass Transf.* 32 (2005) 175–183.
- [30] S.T. Munkejord, H.S. Mæhlum, G.R. Zakeri, P. Neksa, Micro technology in heat pumping systems, *Int. J. Refrig.* 25 (2002) 471–478.
- [31] J.R. Thome, Boiling in microchannel: a review of experiment and theory, *Int. J. Heat Fluid Flow* 25 (2004) 128–139.